Key Engineering Materials
ISSN: 1662-9795, Vol. 926, pp 1986-1992
doi:10.4028/p-sz798f

Submitted: 2021-12-07
Revised: 2022-01-28
Accepted: 2022-02-03
Online: 2022-07-22

Fracture Prediction of Third Generation Advanced High Strength Steels Using Hosford-Coulomb Damage Model

Manuel Jimenez[1,a*], Abel D. Santos[1,2,b], Rui L. Amaral[1,c], Daniel J. Cruz[1,2] and J. Cesar de Sa[1,2]

[1]Institute of Science and Innovation in Mechanical and Industrial Engineering, Porto, Portugal

[2]Department of Mechanical Engineering, Faculty of Engineering, University of Porto, Portugal

[a]mabarca@inegi.up.pt, [b]abel@fe.up.pt, [c]ramaral@inegi.up.pt

Keywords: damage modelling, fracture prediction, finite element method, sheet metal forming.

Abstract. The latest demands in reduction of emissions compel the automobile industry to lighten the structure of vehicles using third generation advanced high strength steels. Due to the novelty of these steels, there is a need to characterize their fracture behavior during the forming process. This paper presents a study of strain field, crack locus and instant of failure for 980 grade third generation advanced high strength steel using defined tests with two specimens. Numerical simulations and experiments have been performed to evaluate and to compare the obtained results for this steel. Numerical simulations with implemented Hosford-Coulomb damage model use the extended finite element method to predict the fracture occurrence. According to results, numerical simulation predicts crack locus similar to experimental tests. Failure of the material shows a high sensitivity to damage evolution law.

Introduction

Advanced high strength steels are widely used in the automobile industry. Demands in emissions reduction have driven the development of third generation of Advanced High Strength Steels (AHSS) with a superior strength/ductility balance that allows to reduce weight in structures [1]. The prediction of the fracture behavior of these novel materials during metal forming process requires the use of numerical tools like finite element software. Numerical simulations enable the implementation of ductile damage models to calculate the degradation of the material and the fracture initiation. Several damage models have been applied over the last years to the forming process of AHSS. The physics-based GTN [2], the phenomenological Johnson-Cook [3] and Hosford-Coulomb damage models [4] have been in the spotlight of recent studies.

Particularly focused on grade 980 third generation of AHSS, the influence of tension test specimen and width-to-thickness ratio on fracture strain has been addressed concluding that specimen geometry, material thickness and measurement of fracture area must be indicated when reporting fracture strains [1]. The forming limits and the work hardening behavior of USS CR980XG3™ AHSS have been determined through several experimental tests and validated with finite element simulations [5].

The use of the extended finite element method (XFEM) to simulate the crack propagation in ductile metals has been mainly applied to micromechanical damage models [6,7]. The method was recently coupled with Cohesive zone modelling in 3D tensile and shear specimens leading to realistic fracture surfaces [8].

This work addresses the prediction of fracture of USS CR980XG3™ AHSS by coupling the phenomenological Hosford-Coulomb damage model with the XFEM method. The objective of this study is to validate the proposed methodology for the prediction of the final fracture state of USS CR980XG3™ AHSS specimens, particularly, a central hole specimen and a shear fracture specimen.

Material Mechanical Behavior

The mechanical properties of USS CR980XG3™ AHSS in the sheet rolling direction are summarized in Table 1 including Young elastic modulus (E), Poisson ratio (ν), yield strength (R_p), ultimate tensile strength (R_m), uniform elongation (e_u) and total elongation (e_t) determined by uniaxial tensile test in specimens of 1.58 mm thickness [5].

Table 1: Mechanical properties of USS CR980XG3™ AHSS [5].

E [MPa]	ν [-]	R_p [MPa]	R_m [MPa]	e_u [%]	e_t [%]
192000	0.289	604	1040	18.0	23.4

Table 2 lists the parameters of the Swift law, modelling the hardening curve of the uniaxial tensile test and the anisotropy ratios represented by Lankford coefficients for 0°, 90° and 45° related to the rolling direction [5].

Table 2: Anisotropic Lankford coefficients and Swift hardening of USS CR980XG3™ AHSS [5].

R-value			Swift parameter (RD – Rolling Direction)		
0°	45°	90°	K	ε_0	n
0.861	0.957	0.895	1880	0.0069	0.231

Constitutive Model for Ductile Fracture

The Hosford-Coulomb damage model is selected to drive the initiation of damage due to its capability to predict the fracture initiation of ductile AHSS with good accuracy [10]. This criterion uses the strain to fracture data provided by four experimental tests (uniaxial, biaxial, pure shear and plane strain) to calculate the overall strain at damage initiation as a function of triaxiality η and the Lode angle Θ:

$$\bar{\varepsilon}_f = b(1+c)^{\frac{1}{n}}\left(\left\{\frac{1}{2}[(f_1-f_2)^a+(f_2-f_3)^a+(f_3-f_1)^a]\right\}^{\frac{1}{a}}+c(2\eta+f_1+f_3)\right)^{-\frac{1}{n}} \quad (1)$$

where the triaxiality η defines the ratio between the hydrostatic stress σ_m and the equivalent stress $\bar{\sigma}$ from von Mises yield function. The trigonometric functions f_1, f_2, f_3:

$$f_1[\bar{\theta}] = \frac{2}{3}\cos\left[\frac{\pi}{6}(1-\bar{\theta})\right] \quad (2)$$

$$f_2[\bar{\theta}] = \frac{2}{3}\cos\left[\frac{\pi}{6}(3+\bar{\theta})\right] \quad (3)$$

$$f_3[\bar{\theta}] = -\frac{2}{3}\cos\left[\frac{\pi}{6}(1+\bar{\theta})\right] \quad (4)$$

introduce the Lode angle Θ which measures the ratio between the second and third stress tensor invariants. The increment of damage is defined according to equation:

$$dD = \frac{d\bar{\varepsilon_p}}{\bar{\varepsilon}_f[\eta,\bar{\theta}]} \quad (5)$$

where $\bar{\varepsilon}_f$ is the strain to fracture of Eq. 1. Assuming D = 0 for the plastically undeformed material, fracture initiates when the damage indicator attains unity (D = 1).

Figure 1 represents strain to fracture data as function of the triaxiality η [9]. The values of fracture in pure shear (η=0.0), uniaxial (η=0.33), plane strain (η=1/√3) and biaxial (η=0.66) are extracted to calculate the parameters a, b, c from Eq. 1. Table 3 provides the Hosford-Coulomb parameters for USS CR980XG3™ AHSS. The parameter n is fixed and defined as 0.1 [6].

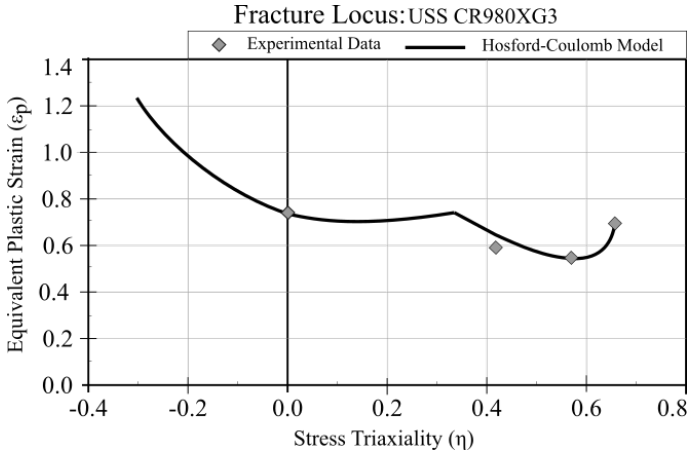

Figure 1: Hosford Coulomb damage model for USS CR980XG3™ (adapted from [9]).

Table 3: Hosford Coulomb damage model parameters for USS CR980XG3™.

HC damage parameter	Value
a	1.5468
b	0.7065
c	0.0361
n	0.1

Experimental Procedure

The specimens were machined from a sheet of material of 1.58 mm thickness. Figure 2 depicts the geometry dimensions of the Central Hole specimen and the Shear Fracture specimen. The strain to fracture for uniaxial tension can be determined from central hole specimens, provided that the hole size is chosen properly [10]. The dimensions of the Shear Fracture specimen are adapted from the proposed geometry for medium ductility steels to guarantee fracture at simple shear loading conditions [12]. Two samples of Central Hole specimen and three samples of Shear Fracture specimen are tested. All specimens are aligned with the rolling direction of the sheet.

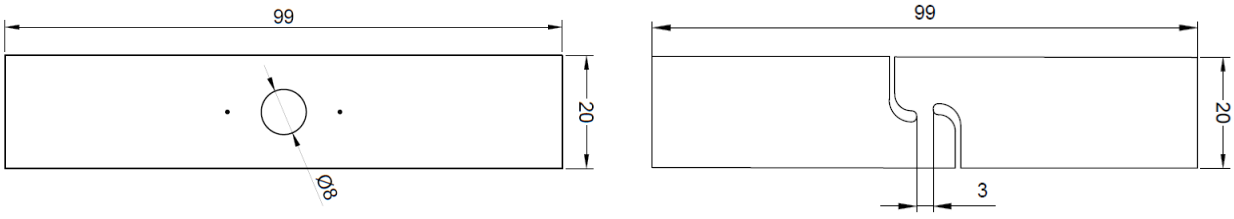

(a) (b)

Figure 2: Dimensions in mm of Central Hole specimen (a) and Shear Fracture specimen (b)

Before testing, the specimens were painted with a high-contrast stochastic speckle pattern of 50 μm size over the area of interest to determinate the strain field by Digital Image Correlation (DIC). Figure 3a shows the painted pattern in one of the samples.

All specimens were tested at a constant crosshead speed of 0.4 mm/min corresponding to a strain rate of 2 x 10^{-4}/s. The tests were performed at room temperature on INSTRON 5900R testing machine

with a 100 kN load cell. A 5 MPixel camera (Basler acA2440-75um, 2448x2048 pixels) in conjunction with a high resolution lens (Fujinon HF50HB-1B, f2.3/50 mm) are employed to take the images at a frequency of 6 and 3 Hz for Central Hole specimen and Shear Fracture specimen, respectively. Figure 3b shows the specimen set-up in the testing machine.

The elongation and the strain field of the specimens were measured by DIC technique using the software VIC2D-Correlated solutions. A subset size of 21 pixels and step size of 5 characterizes the correlation analysis.

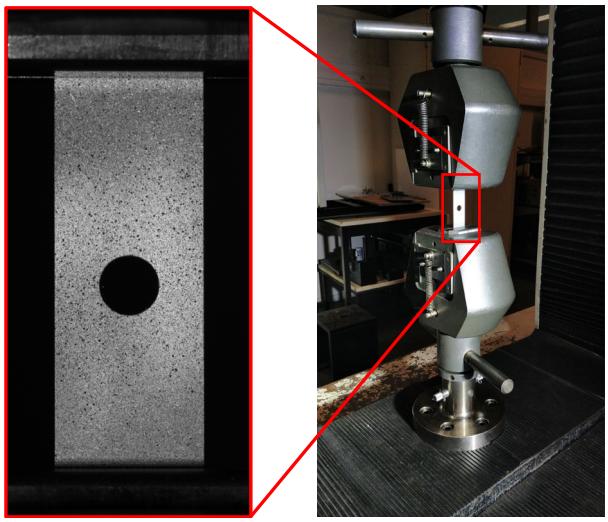

(a) (b)

Figure 3: Speckle pattern (a) and set-up in tensile machine (b) of Central Hole specimen.

Numerical Procedure

The experiments are numerically reproduced using Abaqus Finite Element code. The complete geometries of Fig. 2 are modelled in 3D and the grips are implemented as rigid surfaces attached to the extremes of the model. One of the grips is fixed and the other grip has a displacement at a constant velocity of 1 mm/s in the normal direction to the cross-section of the specimens.

Reduced-integration eight-node 3D solid elements (type C3D8R of the Abaqus element library) are used for the mesh of the models. The elements are uniformly distributed over the area of interest. The area of interest of 20x20 mm^2 around the center of Central Hole model and contains 16 000 elements in 5 layers through thickness. 14 500 elements in 6 layers through thickness are distributed along the area of interest of 5x5 mm^2 of Shear Fracture model. The material model follows Hill'48 yield criterion and an isotropic hardening Swift law, as defined in Table 2.

The numerical process consists of two simulations. First, an explicit dynamic solver is used to calculate the maximum principal strain at damage initiation, according to the Hosford Coulomb damage model of Table 3. Next, an implicit dynamic solver is used to simulate the fracture phenomenon by the extended finite element method. The elements in the area of interest are enriched with asymptotic functions allowing to initiate a crack at any element centroid [13]. The first element that reaches the maximum principal strain reported from the explicit solution initiates the crack. The crack propagates according to the exponential damage evolution law of the form:

$$d = \frac{1-e^{-\alpha(\bar{u}^{pl}/\bar{u}_f^{pl})}}{1-e^{-\alpha}} \tag{5}$$

where d is the damage indicator, $\bar{u}^{pl}$ the effective plastic displacement, $\bar{u}_f^{pl}$ the relative plastic displacement at failure and α the exponent [14]. This evolution law is used due to its flexibility, since the definition of the exponent α allows to calibrate the damage progression of the material. Once the

damage initiation criterion has been reached the effective plastic displacement $\bar{u}^{pl}$ is defined with the evolution equation:

$$\dot{\bar{u}}^{pl} = L\,\dot{\bar{\varepsilon}}^{pl} \tag{6}$$

where L is the characteristic length of the element.

Results and Discussion

Several results are selected to validate the followed numerical procedure with the experimental fracture behavior of USS CR980XG3™. The reaction force, the failure of the material and the crack locus are assessed by the Central Hole specimen. The strain field before fracture is assessed by the Shear Fracture specimen.

Figure 4a shows the force versus elongation curves of the experimental Central Hole specimens. The elongation is given by a virtual extensometer of length 20 mm marked with dots, as seen in Fig. 2a. The force corresponds to the reaction force of the machine grip. The two experimental samples present a similar elasto-plastic response. As for occurrence of fracture, both samples have close elongation to failure.

Figure 4b presents the simulated force versus elongation curves for different exponents in damage evolution law of Eq.5. The models implement the maximum principal strain at fracture extracted from sample 2. The exponent of 0.1 indicates an evolution quasi-linear that leads to a premature failure of the model. The negative exponents define a smooth degradation of the material at the initial stage that allows to delay the failure of the model. An exponent of -8.0 in the damage evolution law fits the failure of sample 2. The model does not predict the steep drop in force from sample 2, which is controlled by the relative plastic displacement at failure in Eq. 5. A value of 0.0 indicates instantaneous failure [14]. The model considers a displacement at failure of 0.2 mm, minimum allowed by solution convergence.

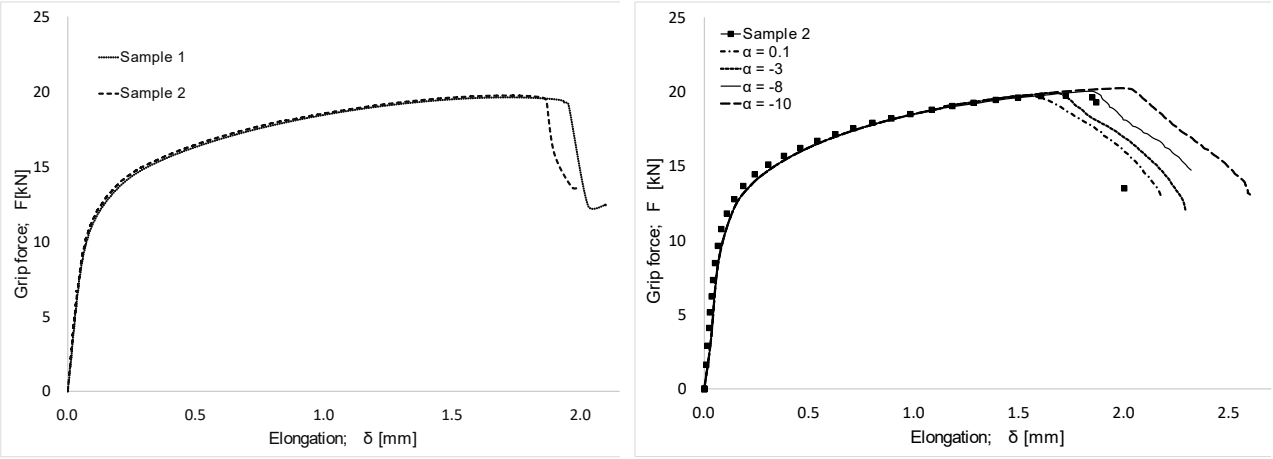

(a) (b)

Figure 4: Force-elongation from experiments (a) and numerical models with different damage evolution laws (b) in Central Hole specimen.

Figure 5a shows the state of Central Hole specimen after fracture initiation. The crack is located in one of the bridges slightly upper the critical section of the geometry. Figure 5b shows the crack location of the numerical model implementing the extended finite elements method. Crack propagates parallel to the cross section of the model gradually partitioning the elements presented in Fig. 5c.

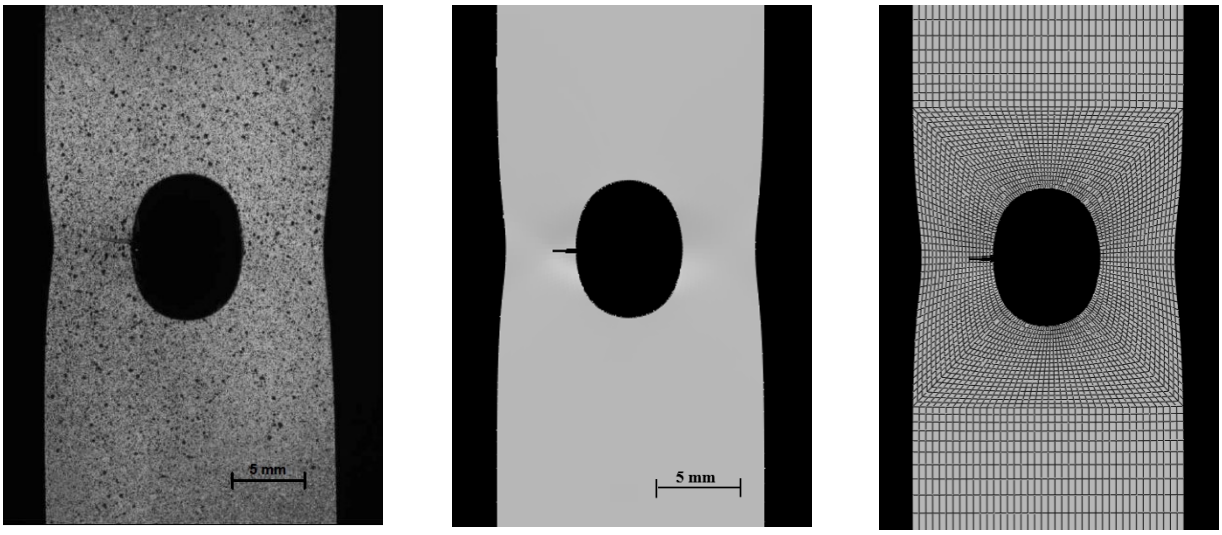

(a) (b) (c)

Figure 5: Crack locus on Central hole specimen sample 2 (a) and numerical model (b). Finite element mesh (c).

The state of the Shear Fracture specimen before crack occurrence is analyzed in Fig. 6, which plots the strain field previous to fracture. In particular, the major principal strains are compared for sample 1 (Fig. 6a) and numerical model (Fig. 6b). Both contours present the maximum strains at the region between the two notches with the model predicting a maximum strain of 0.56 while the experimental maximum value shows 0.635. The extrapolation for high values of deformation in tensile-based hardening law may cause the difference in magnitude of strains. The strain fields show similar limits for undeformed region. The deformed shape of the notches follows a similar profile.

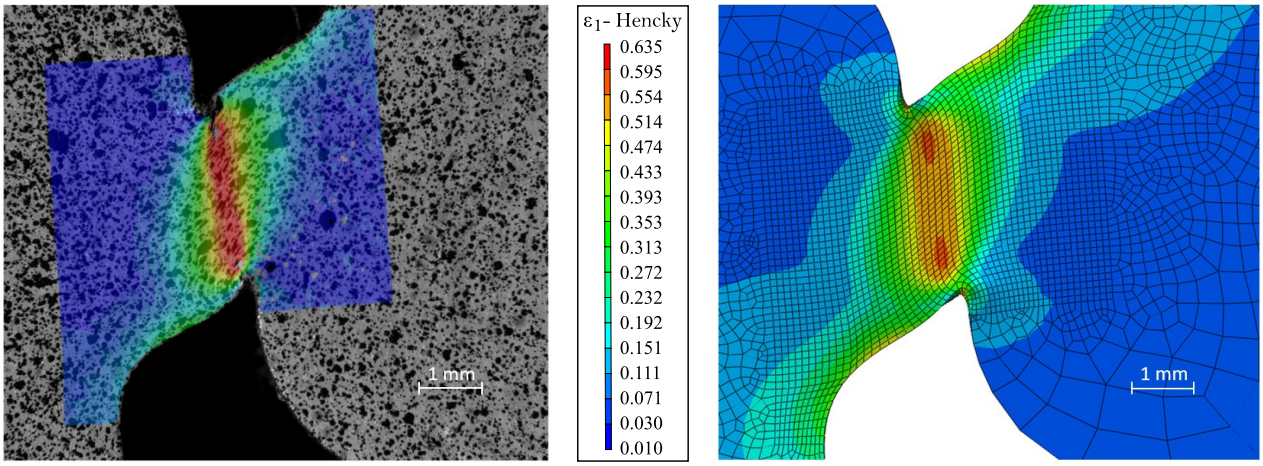

(a) (b)

Figure 6: Major principal strain field before fracture for sample 1 (a) and numerical model (b) in Shear Fracture specimen.

Conclusions

In this paper, two specimens of 980 grade third generation advanced high strength steel are used to validate implementations in fracture models. Digital image correlation is used to extract the displacement and strain evolution of Central Hole specimen and Shear Fracture specimen. In parallel, Hosford-Coulomb damage model is implemented in a simulation process that includes the extended finite element formulation. The failure of Central Hole specimen is evaluated by different damage evolution laws. Calibrated model predicts the instant of failure but misses to reproduce the instantaneous loss of the load- carrying capacity in experimental samples. Crack initiation locus and shape present a good agreement in Central Hole specimen. The strain field previous to fracture is

assessed in Shear Fracture specimen resulting in similar distribution with difference in the magnitude of the strains. Further development of numerical models to address instantaneous failure, crack direction during propagation, and triaxiality analysis will be put into effect in future studies.

Acknowledgments

The authors gratefully acknowledge the support of General Motors and U. S. Steel for supplying the material investigated in this work Also, it is greatly acknowledged the financial support of the Portuguese Foundation for Science and Technology (FCT) under the Project POCI-01-0145-FEDER-032466 (PTDC/EME-EME/32466/2017) – NanosFLiD – Formability of Third Generation Advanced High Strength Steels, by UE/FEDER through the program COMPETE 2020.

References

[1] B. Hance, Advanced High Strength Steel (AHSS) Performance Levels. SAE Int. J. Mater. Manf., 11(4) (2018) 505-516.

[2] K. Achineethongkham, V. Uthaisangsuk, Analysis of forming limit behaviour of high strength steels under non-linear strain paths using a micromechanics damage modelling. Int. J. of Mechanical Sciences, 183 (2020).

[3] R. Amaral, A. D. Santos, J. César de Sá, S. Miranda, Formability prediction for AHSS materials using damage models. J. of Physics: Conference Series, 843 (2017).

[4] B. Erice, C. C. Roth, D.Mohr, Stress-state and strain-rate dependent ductile fracture of dual and complex phase steel. Mech. of Materials, 116 (2018) 11–32.

[5] R. O. Santos, L. P. Moreira, M. C. Butuc, G. Vincze and A. B. Pereira, Damage Analysis of Third-Generation Advanced High-Strength Steel Based on the Gurson–Tvergaard–Needleman (GTN) Model. Metals, 12(2) (2022) 214.

[6] M. I. M. Ahmad, J. L. Curiel-Sosa, S. Arun and J. A. Rongong, An enhanced void-crack-based Rousselier damage model for ductile fracture with the XFEM. Int. J. Damage Mechanics, 28 (2018).

[7] S. Beese, S. Loehnert and P. Wriggers, 3D ductile crack propagation within a polycrystalline microstructure using XFEM. Computational Mechanics, 61(1–2) (2018) 71–88.

[8] K. Nikolakopoulos, J. P. Crété, P. Longère, Progressive failure of ductile metals: Description via a three-dimensional coupled CZM–XFEM based approach. Eng. Fracture Mechanics, 243 (2021).

[9] U. S. Steel, https://www.ussteel.com/customers/products/advanced-high-strength-steel, 12/2021.

[10] C. C. Roth, & D. Mohr, Ductile fracture experiments with locally proportional loading histories. Int. J. of Plasticity 79 (2016) 328–354.

[11] D. Mohr, S. J. Marcadet. Micromechanically-motivated phenomenological Hosford–Coulomb model for predicting ductile fracture initiation at low stress triaxialities. Int. J. of Solids and Structures, 67-68 (2015) 40–55.

[12] C. C. Roth and D. Mohr, Determining the strain to fracture for simple shear for a wide range of sheet metals. Int. J. of Mechanical Sciences, 149 (2018) 224–240.

[13] T. Belytschko and T. Black, Elastic crack growth in finite elements with minimal remeshing. International Journal for Numerical Methods in Engineering, 45(5) (1999) 601–620

[14] Simulia user manual:
https://help.3ds.com/2019/english/dssimulia_established/simacaematrefmap/simamat-c-damageevolductile.htm?contextscope=all, access on 12/2021.